metals

MDPI

Article

Effect of Pressure on Densification and Microstructure of W-Cr-Y-Zr Alloy during SPS Consolidated at 1000 °C

Huijuan Zhu [1], Xiaoyue Tan [1,*], Qingbo Tu [1], Yiran Mao [2,3], Zelin Shu [1], Jie Chen [2], Laima Luo [1,4], Andrey Litnovsky [2], Jan Willem Coenen [2,5], Christian Linsmeier [2] and Yucheng Wu [1,4]

1 School of Materials Science and Engineering, Hefei University of Technology, Hefei 230009, China
2 Forschungszenturn Jülich GmbH, Institut für Energie-und Klimaforschung–Plasmaphysik, Partner of the Trilateral Euregio Cluster (TEC), 52425 Jülich, Germany
3 School of Mechanical Engineering, Hefei University of Technology, Hefei 230009, China
4 National-Local Joint Engineering Research Center of Nonferrous Metals and Processing Technology, Hefei University of Technology, Hefei 230009, China
5 Department of Engineering Physics, University of Wisconsin-Madison, Madison, WI 53706, USA
* Correspondence: xytan@hfut.edu.cn

Abstract: During the spark plasma sintering (SPS) consolidation process, the pressure affects the densification and microstructure evolution of the sintered body. In this paper, the W-Cr-Y-Zr alloy powder was heated to 1000 °C under different applied pressure conditions using spark plasma sintering process, and the effect of pressure on the densification process and microstructure was analyzed. Due to the low sintering temperature, the crystalline size of all the produced W-Cr-Y-Zr alloy is less than 10 nm, which is close to that of the original powders. Cr-rich phase can be detected in the sintered samples due to spinodal decomposition. It is found in this work that the external pressure will increase the contact area between the powder particles, resulting in a higher local pressure at the particle contact, which promotes densification by sliding between the particles under the condition of softening of the particle surface. Additionally, according to the viscous flow theory, the viscous flow activation energy decreases with the increase of pressure. This is because the pressure provides additional driving force to the powder viscous flow process and accelerates the powder shrinkage.

Keywords: spark plasma sintering; pressure; densification; viscous flow; Cr-rich phase; crystalline size

Citation: Zhu, H.; Tan, X.; Tu, Q.; Mao, Y.; Shu, Z.; Chen, J.; Luo, L.; Litnovsky, A.; Coenen, J.W.; Linsmeier, C.; et al. Effect of Pressure on Densification and Microstructure of W-Cr-Y-Zr Alloy during SPS Consolidated at 1000 °C. *Metals* **2022**, *12*, 1437. https://doi.org/10.3390/met12091437

Academic Editor: Pasquale Cavaliere

Received: 20 July 2022
Accepted: 26 August 2022
Published: 29 August 2022

1. Introduction

Self-passivating tungsten alloys (SPTAs), as a functional material with high melting point, high hardness, and good oxidation resistance, are the first-wall materials developed for future nuclear fusion devices in case of loss-of-cooling accident (LOCA) [1]. Currently, the main SPTAs systems are W-Cr-Ti/Y/Zr systems [1–4]. Under high-temperature oxidizing environments, the alloying elements added to SPTAs form dense oxide skins on their surfaces, inhibiting the generation of the volatile, radioactive WO_3 [1]. Y forms nano-Y_2O_3 particles distributed at grain boundaries, inhibiting the grain growth [5]. Studies have shown [3–5] that the addition of appropriate amounts of Y to SPTAs can effectively reduce the oxidation rate. Zr will form ZrO_2 particles that act as nucleation sites for initial oxide growth, strengthen the interfacial strength between the matrix and oxide, prevent the diffusion of Cr cations, and prolong the oxidation time [6]. In addition, it has been shown [7,8] that the higher the density of SPTAs, the smaller the grain size and the more homogeneous the organization (no Cr-rich phase), the better their antioxidant properties.

Concerning the SPTAs studies, some researchers have been devoted to improving the properties of thermal shock resistance [5], irradiation resistance [9] and oxidation resistance [7], and the others [3,9] have been committed to the preparation processes to obtain SPTAs with excellent performance. For the preparation of SPTAs, the main route is via powder metallurgy processes [10]. The spark plasma sintering (SPS) technique using

the Joule heating by electric current and external pressure can densify the powders in a short time and, hence, suppress the grain growth [11]. It is widely used in the preparation of difficult-to-sinter materials, such as refractory metals and ceramics [12]. Due to the short sintering period, the use of SPS for the preparation of SPTAs is easy to achieve dense bulk materials with fine-grains and homogeneous microstructure [13], which will be beneficial to improve the antioxidant properties of SPTAs [14].

The effect of pressure, as one of the main sintering parameters, has been extensively studied for SPS process [15–17]. Wang et al. [18] sintered TiAl alloys using the SPS technique and analyzed the densification process. It was found that sintering at 900 °C, the powder particles undergo plastic deformation due to the applied pressure, resulting in flattening of contact areas and reduced porosity, causing densification. While the temperature is over 900 °C, diffusion acts as the dominant mechanism of densification, where the local stress at the sintering neck can increase diffusion channels and enhance densification, and this diffusion process mainly involves grain boundary diffusion. The powder consolidation process can usually be summarized in two steps: densification and grain growth [19]. Yang et al. [20] used field-assisted sintering technology (FAST, another name for SPS) to prepare W-Cr-Y-Zr alloys and gives the effect of applied pressure for the whole sintering process, including both stages. It reported that the pressure changes the internal "local overheating" behavior, which affects the Cr-rich phase content. In order to figure out the pressure effect more clearly, the densification and grain growth stages need to be discussed separately for better controlling and optimizing the production process.

This work focuses on the influence of pressure on the densification procedure. Here, the SPS technique was used to sinter W-Cr-Y-Zr self-passivating alloy powders at a sintering temperature of only 1000 °C in order to analyze the corresponding densification mechanisms for the densification stages where the grains have not grown significantly. The sintering pressure were changed from 50 to 90 MPa. A viscous flow model was used to evaluate the effect of SPS pressure on the mechanisms associated with the densification stage of the powder, and additionally its effect on the microstructure of the W-Cr-Y-Zr alloy was investigated.

2. Experimental

2.1. Sample Preparation and Characterization

In this work, SPTAs bulk samples were prepared by powder metallurgy route, including two steps of mechanical ball milling and SPS consolidation. The equipment used was a planetary ball mill (QM-3SP4, Nanda Instruments, Nanjing, China) and SPS equipment (Labox-350, NJS Co., Ltd., Yokohama, Japan), respectively. The starting powders were W powders (99.9%, 5 μm), Cr powders (99.9%, 74 μm), Y powders (99.5%, 74 μm), and ZrH_2 powders (99.9%, 74 μm). The selected powders were firstly mixed based on the composition of W-11.4Cr-0.6Y-0.4Zr (wt.%), and then were encapsulated with WC grinding balls (Ø10 mm) in an Ar atmosphere with a ball-to-material ratio of 5:1. A planetary ball mill was used for 64 h at the speed of 225 rpm/min. WC grinding balls (Ø10 mm) were then replaced to Ø5 mm WC grinding balls, followed by a milling process for 10 h. The milled powders were randomly taken and characterized by X-ray diffraction (XRD, X' Pert PRO MPD, Cu target, Eindhoven, The Netherlands). X-ray diffraction was scanned from 30° to 90°, scanning speed was 6°/min. Figure 1 shows the XRD pattern of the milled powders. It can be determined that the W-Cr-Y-Zr alloy powders after mechanical milling has a body-centered cubic structure. In addition, the pattern shows an obvious double-peak structure, which indicates that there are two components of W-Cr matrix phase.

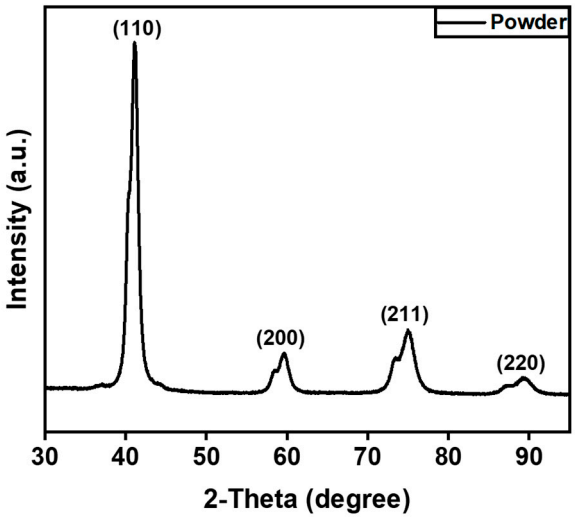

Figure 1. XRD pattern of the W-Cr-Y-Zr powders after mechanical milling.

After the ball milling process, the powders were sintered by SPS. Combined with the previous study [21], the sintering temperature designed in this work is 1000 °C. The loading pressure is 30, 50, and 90 MPa, respectively. The specific sintering process is shown in Figure 2a. Thermocouples were used to measure temperature change, and the detection point is halfway down the radial direction of the die. The sample height designed is ~5 mm, and the diameter is 13 mm. A carbon paper with a thickness of 0.05 mm is padded between the powders and the die/punches to ease the demolding after sintering. A boron nitride insulating layer was sprayed on the side of the carbon paper in contact with the die so that the current flows only through the powders, hence, a designed current density can be achieved. In addition, a tungsten foil with a thickness of 0.05 mm was placed between the carbon paper and the sample in order to slow/stop carbon contamination during the sintering process [22]. The powders were compacted before sintering with a pressure of 10 MPa. The SPS processes were performed in vacuum with a pressure below 20 Pa. To reflect the real variation of the sample height, the process with the same parameters was also applied to only graphite molds as a reference. Parameters such as time, current, pressure, and displacement were recorded by the SPS system every second.

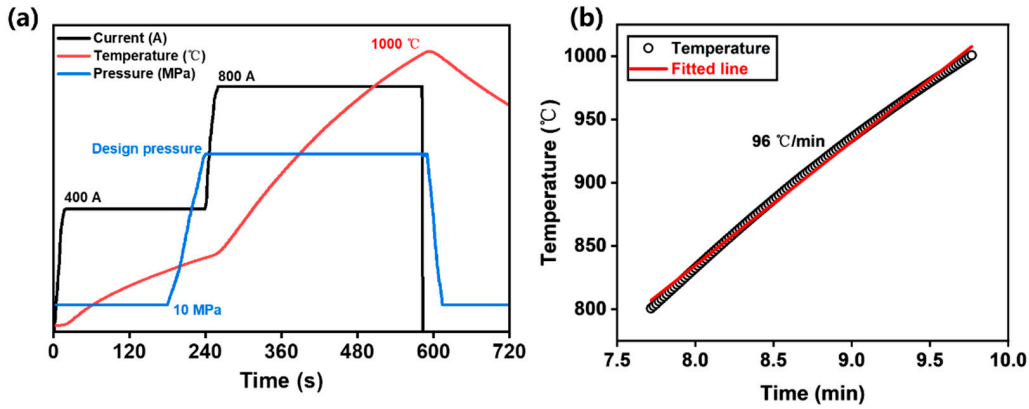

Figure 2. W-Cr-Y-Zr alloy (**a**) sintering process curve; (**b**) temperature rise curve at 800–1000 °C.

The sintered samples were mechanically ground with different grades of silicon carbide paper for density measurement. The fracture morphology was analyzed by field emission scanning electron microscopy (Gemini 300, Sigma Zeiss, Jena, Germany) to characterize the material microstructure. The phase constitutions of the sintered samples were also characterized by XRD with the same parameters for the powders. The Debye

Scherrer equation and the fracture morphology of the samples were used to evaluate the crystalline size in the particles. In addition, to visually clarify the microstructure evolution in the W-Cr-Y-Zr sample with different pressure, the cross-sections of samples were also characterized by SEM and energy dispersive X-ray spectroscopy (EDX). The detailed information about the preparation process for cross section characterization are described in our previous work [23].

2.2. Density Measurement and Calculation

To clarify the densification behaviors of the samples during the SPS process, the corresponding density change was evaluated. The density of the sample is equivalent to the sample height variation, which is macroscopically related to the displacement of the graphite punches, and was recorded by the SPS facility during the sintering process. Notably, the punches' displacement also involves expansion and shrinkage. Therefore, the actual height variation of the sample is obtained by subtracting the punches expansion obtained from the reference experiment. The instantaneous density (ρ_i) can be calculated from the instantaneous height of the sample by the following equation.

$$\rho_i = \frac{H_f}{H_i}\rho_f \quad (1)$$

where H_i is the instantaneous height of the sample, H_f is the final height of the sample, and ρ_f is the final density of the sample.

Considering low sintering temperature (1000 °C), the final density of the sintered samples is low with substantial open pores. Archimedes' method is not efficient to measure the material density for such a condition [24]. Therefore, a geometric/gravimetric method was used to measure the overall material density for the as-sintered samples. The instantaneous relative density is defined as the ratio of the instantaneous density and the theoretical density. The theoretical density was calculated by the same method in our previous study [21]. After calculation, the theoretical density of W-11.4Cr-0.6Y-0.4Zr alloy is 15.5 g/cm^3.

3. Results and Discussion

3.1. Densification Process

The densities of the samples are calculated from Equation (1), and the relative density is defined as the ratio of actual density to theoretical density. Figure 3a shows the change curves of relative density of W-Cr-Y-Zr alloy with sintering temperature under different sintering pressures. It can be seen that with the increase of applied pressure, the curve shifts towards the low temperature region, indicating that the applied external load can effectively enhance the densification process. Combining the density change and the corresponding densification mechanisms, the densification curve of W-Cr alloy shows a typical "S" shape, which consists of three main stages [25], i.e., the initial slow densification stage, where the relative density below 70%, and the dominant densification mechanism is particle displacement; subsequently fast densification stage that sintering necks formation and growth; and the final slow densification stage, where the relative density over than 90%, and the densification dominated by grain boundary diffusion. Based on the "S" curve model [26], the densification curves were fitted and are shown in Figure 3a. It can be seen that the sintering process in this study belongs to stage II of the fast densification stage. According to the density change, the variation of densification rate ($\frac{d\rho}{dt}$) with temperature for the samples at different pressures was also plotted, as shown in Figure 3b. The densification rate denotes the instantaneous displacement of the sample during the sintering process. Obviously, the densification rate of the sample increases with the increase of pressure. It is worth noting that the densification rate of the sample with the applied 90 MPa load is less than zero before 500 °C. From Figure 3a, the applied pressure of 90 MPa has led to the powder compact with a high density of 68% at 400 °C. It is hard to further the dense particle displacement below 500 °C, therefore, the powder displacement was

dominated by thermal expansion, where the densification rate exhibits negative value. In addition, in Figure 3b, the densification rate curves under different pressures intersect at a point before 600 °C, which is possibly related to the densification mechanism of W-Cr alloy at different stages. In our previous work [21], the critical temperature divided the slow densification stage, and the fast densification stage is approximately 600 °C, which is similar to the formation temperature of sintering necks. The formed sintering necks will provide enough paths for atomic diffusion and enhance the densification process [27].

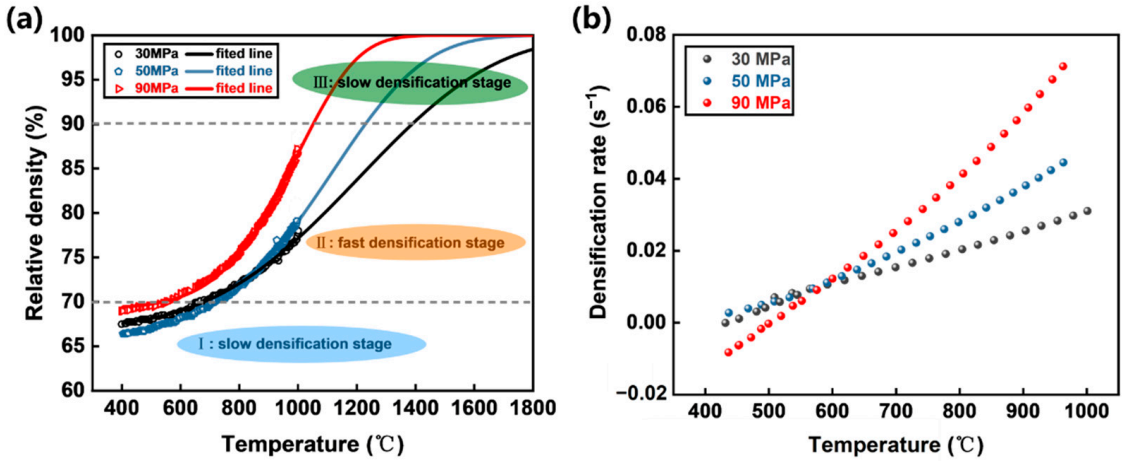

Figure 3. (**a**) W-Cr-Y-Zr bulk densification curve; (**b**) densification rate curve.

3.2. Microstructure and Phase Constitution

Figure 4 shows the cross-sections at of the samples sintered at different pressures. It can be seen that several unclosed pores still exist in the sample sintered at 30 MPa, and the pores gradually disappear as the pressure increases. This finding agrees with the density change, as shown in Figure 3. In addition, a few dark grey regions (as denoted with white arrows) embellish in the main grey region. Combined with the EDX characterization, the grey region is the W-Cr matrix, and the dark grey regions are the Cr-rich phases. Notably, the Cr-rich phase in case of the sample sintered with 30 MPa exhibits ribbon patterns, which is similar to the W-Cr-Zr samples interruptedly sintered at 600 °C and 800 °C in our previous study [21]. It supposes that the pattern of Cr-rich phases is related to the "local overheating" was occurred at the regions of pores and cracks. With the pressure increasing, the Cr-rich phases mainly distribute at the contacting areas between the particles, i.e., sintering necks. Combined to our previous analysis in [20], it indicates that the pressure also effects the Cr-rich phase distribution during the intermediate sintering stage.

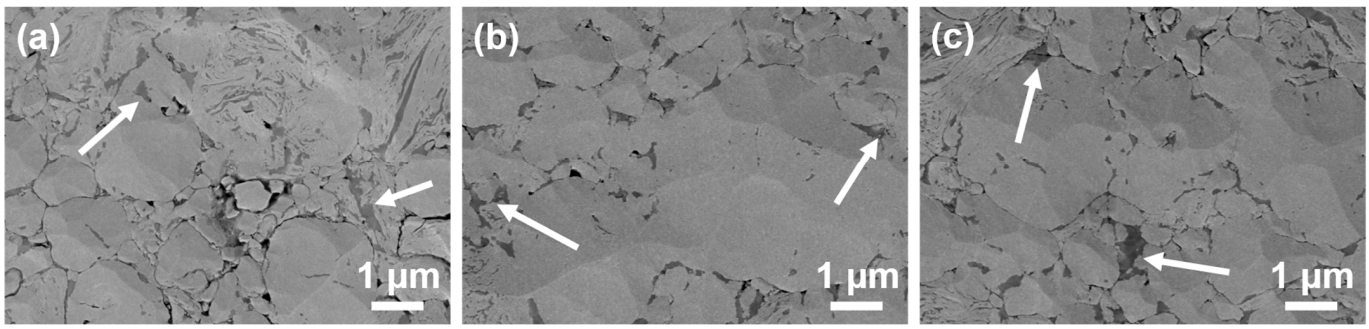

Figure 4. The cross-sections of W-Cr-Y-Zr samples sintered with different pressures. (**a**) 30 MPa; (**b**) 50 MPa; (**c**) 90 MPa. The arrows denote the Cr-rich phases.

The XRD pattern of the W-Cr-Y-Zr alloys after sintering is given in Figure 5a. It shows that the W-Cr-Y-Zr alloy bulk has a body-centered cubic structure. The corresponding

characteristic peaks of Y and Zr elements were not detected because their contents were below the detection limit of the XRD instrument. It is noteworthy that next to the main peak (110) of each sample, a weak characteristic peak appears, which is analyzed to be the precipitated Cr-rich phase. Zooming in on the main peak (110), as shown in Figure 5b, the main peak shifts to the left as the applied pressure increases, near the peak of the pure W phase. This indicates an increase in the lattice constant of the W-Cr matrix with increasing sintering pressure, which is attributed to the precipitation of Cr atoms with small lattice constants from the solid solution in the matrix during the sintering process. In addition, Figure 5c is an enlarged view of the characteristic peak of the Cr-rich phase, which is shifted to the right with increasing applied pressure, i.e., the concentration of Cr atoms in the Cr-rich phase increases. It proposes the result illustrated in Figure 5b.

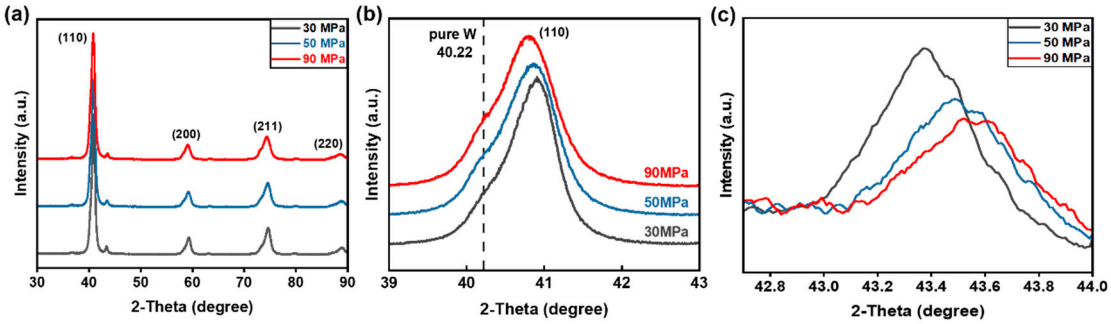

Figure 5. (**a**) XRD pattern of W-Cr-Y-Zr alloys; (**b**) (110) local magnification of the characteristic peak; (**c**) local magnification of the characteristic peak of Cr-rich phase.

According to the W-Cr phase diagram [8], as shown in Figure 6, the Cr precipitation behavior in W-Cr matrix alloys is related to the temperature. In this work, the W-Cr-Y-Zr samples sintered at 1000 °C, which is the intermediate sintering stage in case of our previous study [20] sintered at 1400 °C. From Figure 6, the solution temperature of W-11.4Cr alloy is about 1563 °C. When the sintering temperature was 1000 °C, and the sample temperature would not exceed the solid solution temperature [8], the W-11.4Cr-0.6Y-0.4Zr alloy undergoes spinodal decomposition. It means that the Cr-rich phase can be easily detected, as evidenced in Figures 4 and 5. In case of sintering at 1400 °C (the actual temperature is higher), the formed Cr-rich phase prefers to re-dissolve into W-Cr matrix. Therefore, it is hard to detect the Cr-rich phase using the XRD patterns [20].

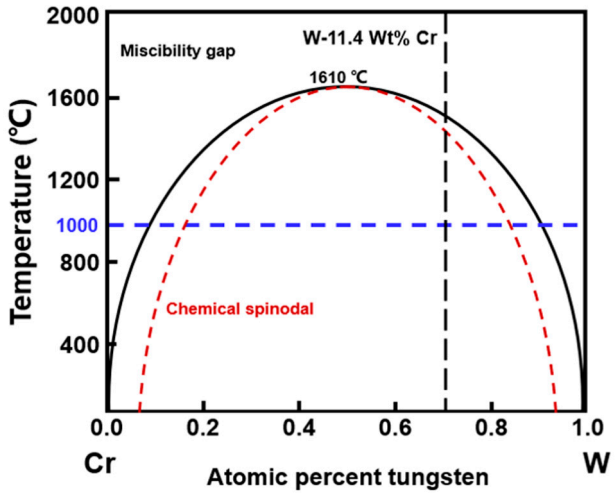

Figure 6. W-Cr binary phase diagram [8]. The black line represents the miscibility gap, and the red dotted line represents the chemical spinodal decomposition region.

Notably, the measurement point of the thermocouple only reaches half the thickness of the graphite die, therefore, there is a difference between the detection temperature and the actual temperature of the sample. Higher pressure means better contact between the powder compact and graphite die, resulting in a lower contact resistance and therefore a corresponding reduction in the temperature difference [28,29]. It indicates the sample loaded with a high pressure, and the corresponding actual temperature below that with a low pressure. The higher the pressure applied, the lower the real temperature of the sample is, and the higher Cr concentration in Cr-rich phase is formed.

In addition, the crystalline size of the samples was calculated based on the XRD data by using the Debye Scherrer formula, as follows [30]:

$$D_{hkl} = \frac{k\lambda}{\beta \cos \theta_{hkl}} \quad (2)$$

where k is the Scherrer constant, usually taken as 0.89, λ is the wavelength of the X-ray, which is 1.54056 Å. β is the half-peak height and width of the diffraction peak, and θ_{hkl} is the Bragg diffraction angle. D_{hkl} is the average crystalline size in the grain plane. Based on the different crystal planes of (110), (200), (211), and (220), the grain size of samples is calculated. The results show that the average crystalline size for 30 MPa, 50 MPa, 90 MPa, and the original powder are: 8.2 ± 2.2 nm, 6.9 ± 1.6 nm, 6.0 ± 3.5 nm, and 5.6 ± 1.3 nm, respectively.

Figure 7 shows the fracture morphologies of the samples after sintering at different pressures. It can be seen that their grain sizes are very small and do not exceed 10 nm, which is consistent with the calculated results of the XRD. Notably, there is only a slight difference in grain size between the samples after sintering with different pressures and the original powders. It indicates no obvious grain growth of the samples during the sintering process. Essentially, the grain growth originates from the atom diffusion, which is related to the temperature and time. Temperature means the drive force for atom diffusion, and time relates to the diffusion distance. In this work, the samples sintered at a low temperature of 1000 °C with a few minutes, which limits the atom diffusion process. In addition, it has reported that the grain growth of W-Cr based alloys is closely related to the bulk density [11]. An obvious grain growth will occur at the relative density over than 90%. It belongs to the sintering stage III, as pointed in Figure 3a. The main densification mechanism at the sintering stage III is grain boundary diffusion, which determines the grain growth of alloys. According to the density measurement, the maximum density of the sintered samples is only 87%. Porosity makes gaps for the atomic diffusion, limiting the grain growth [11,31,32].

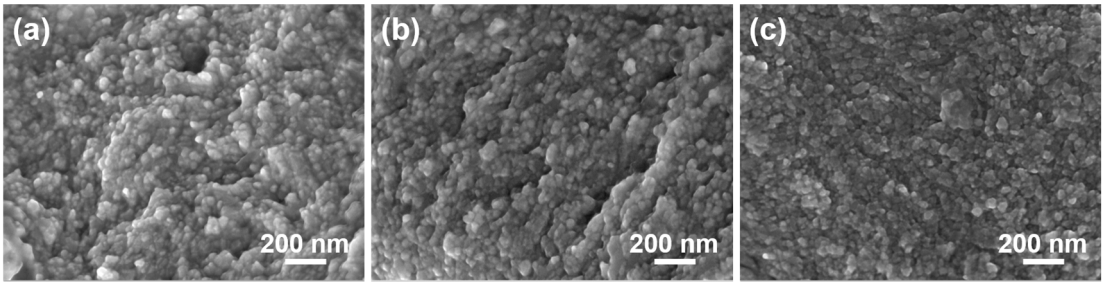

Figure 7. Microstructure of fractures of W-Cr-Y-Zr samples sintered with different pressures: (**a**) 30 MPa; (**b**) 50 MPa; (**c**) 90 MPa.

3.3. Densification Kinetic

When the SPS technique is used to consolidate SPTA powders, the pulsed DC current will preferentially and rapidly pass through the surface of the powder particles, and the temperature of the surface of the powder particles becomes higher than its internal temperature for a short period of time, resulting in the surface softening of the powder

particles [33]. In addition, the higher temperature also leads to a greater atomic disorder on the surface of the particles, and thus the powder particles approach fluid properties during sintering. What is more, Li et al. [34] pointed out that when nanocrystalline materials are sintered, the grain boundaries (at the particle contacts) are amorphous regions, and viscous flow occurs during densification, which can be evaluated using viscous flow theory [35,36]. Therefore, we evaluated the densification process of powder sintering of SPTAs based on the viscous flow theory established by Frankel.

Frankel's viscous flow theory states that when there is no applied load or no need to consider the effect of applied load on densification, the shrinkage behavior of the powder can be expressed as [37]:

$$\frac{\Delta H}{H_0} = \frac{3\gamma}{4L\eta}t \tag{3}$$

where $\frac{\Delta H}{H_0}$ is the displacement change during the sintering of the sample, representing the shrinkage behavior of the powder sample; H_0 is the powder compaction height in mm; ΔH is the displacement change of the powder sample in mm; η is the coefficient of viscous flow, reflecting the degree of viscosity of the powder particles in Pa·s; γ is the particle interfacial energy in J/mm^2; L is the average particle size of the powder.

In this paper, pressure exerts an additional driving force on the densification process and promotes densification. With the effect of pressure considered, Equation (3) can be modified as follows [34]:

$$\frac{\Delta H}{H_0} = \left(\frac{\gamma}{L} + BP\right)\frac{3t}{4\eta} \tag{4}$$

where P is the external load; B is related to the powder properties, including the geometry of the powder particles, powder particle size, etc., dimensionless. The first term (γ/L) in the above equation in parentheses can represent the interfacial driving force, while the second term (BP) can represent the additional driving force related to the external load. In a certain temperature interval range, η is only influenced by temperature and has the Arrhenius relation [38]:

$$\eta = \eta_0 \exp\left(\frac{Q}{RT}\right) \tag{5}$$

where η_0 is the viscous flow coefficient; Q is the activation energy of viscous flow; R is the ideal gas constant (8.314 kJ/mol); T(K) is the absolute temperature. Here, the relationship between temperature and time can be considered as linear, as shown in Figure 2b, so that the temperature T and time t follow the following relationship [39]:

$$\frac{dT}{dt} = c \tag{6}$$

c represents the heating rate of temperature, here 96 °C/min. Combining Equations (3)–(6), the two ends of Equation (4) differentiate for T, the contraction behavior of the powder can be expressed as [34]:

$$\frac{d\left(\frac{\Delta H}{H_0}\right)}{dT} = \left(\frac{\gamma}{L} + BP\right)\frac{3}{4c\eta_0}\exp\left(-\frac{Q}{RT}\right) \tag{7}$$

Taking the logarithm for both ends of (7), we have [34]:

$$\ln\left(\frac{d\left(\frac{\Delta H}{H_0}\right)}{dT}\right) = \ln\left(\frac{3\left(\frac{\gamma}{L} + BP\right)}{4c\eta_0}\right) - \frac{Q}{RT} \tag{8}$$

According to Equation (8), the activation energy of viscous flow can be expressed by the slope of the $\ln\left(\frac{d\left(\frac{\Delta H}{H_0}\right)}{dT}\right) - 1/T$ function, as shown in Figure 8. From Figure 8, it can be seen that the activation energy of viscous flow required for powder densification decreases

with the increase of the applied pressure. Under a pressure of 90 MPa, the corresponding activation energy is 37.6 kJ/mol. The decrease of activation energy implies the pressure plays key roles on the densification process.

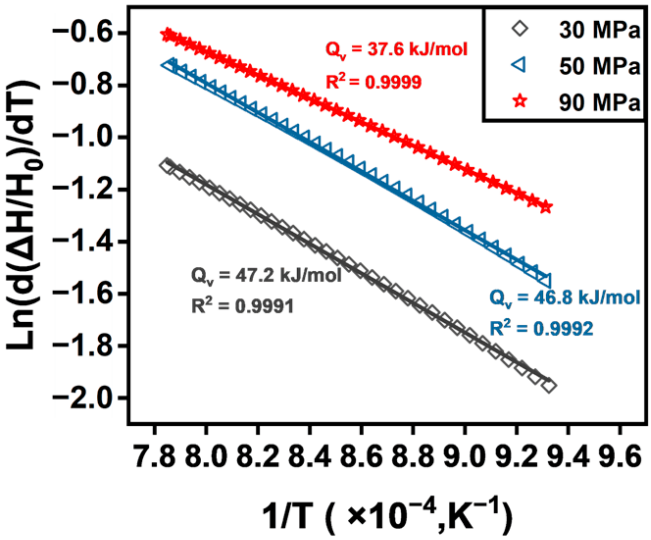

Figure 8. Viscous flow activation energy of the W-Cr-Y-Zr samples sintered with different pressures.

There are at least three actions of pressure on the powders during the SPS process. Firstly, pressure can act as a driving force for plastic deformation and enhance powder displacement. Secondly, as claimed previously, SPS technique will benefit softening the surface of powders. When the current is conducted between powder particles in contact with each other, it passes through a very narrow contact zone of the powder particles (sintering neck). Therefore, the current is forced to flow through the sintering neck in a concentrated manner, i.e., current crowding [40]. This leads to more Joule heat at the sintering necks, which has a higher temperature compared to the other areas, i.e., "local overheating" [41]. Loading a high pressure will ease the local overheating at the particle contacts, resulting in a uniform softened status in powder beds that can be attributed to the viscous flow of the compact. The pressure applied on this basis will bring a larger contact area to the powder particles and a more effective filling between the particles, providing more channels for atomic diffusion and thus further promoting densification. Lastly, when a larger pressure is applied and the local pressure at the powder particle contact is greater, the interparticle contact area will become larger, i.e., the total surface area of the system will decrease, the interfacial energy required for the action of the particle surface tension (under the action of surface tension, the powder particles will undergo a flow similar to that of a viscous liquid) is reduced. Therefore, we suppose that the part of the reduction of the activation energy is brought about by the reduction of the total surface area of the system caused by the pressure acting on the particle surface. Above all, the application of higher pressure will be more favorable to the densification of the powders.

Figure 9 shows the low magnification fracture morphology of samples after sintering with different pressures. The yellow arrows denote the sintering neck, and the dashed line outlines the large particles on the fracture surface. Different to the milled powders, all three samples have been deformed. It supports that the action of pressure enhancing the plastic deformation of the powders. The large particle fractures indicate the crack propagation traversing the powder particle. The small particle fractures would be the appearance of sintering necks after cracking. Combined with the small size of the sintering necks shown in Figure 9, this means that a poor inter-particle bonding and the particles easily slide [41,42]. This process involves the particle displacement under pressure and the subsequent densification mechanism of particle sliding, i.e., it exhibits near-fluid behavior.

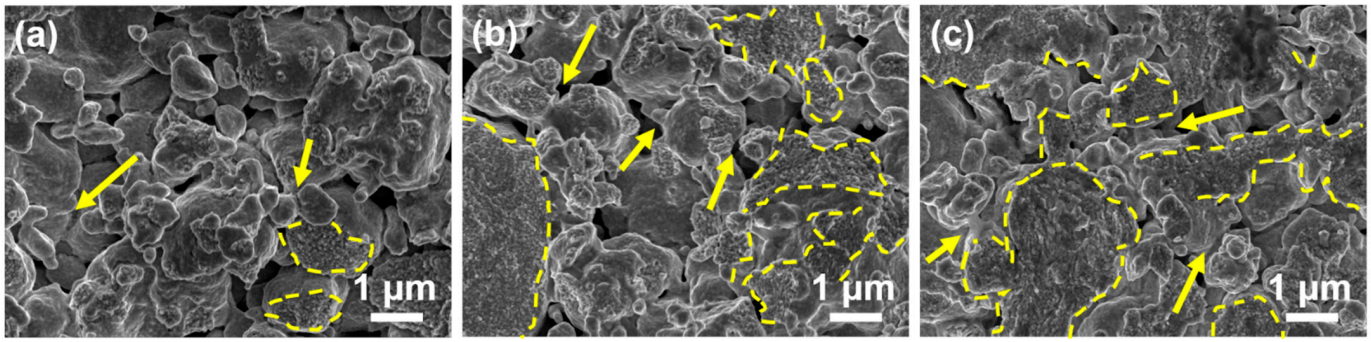

Figure 9. Fracture morphology of W-Cr-Y-Zr samples after sintering at 1000 °C and different pressures: (**a**) 30 MPa; (**b**) 50 MPa; (**c**) 90 MP. The arrows denote the sintering necks, and the dashed lines outline the large particles on the fracture surface.

4. Summary

In this paper, we studied the effect of SPS pressure on the fast densification stage of the sintering process, where the grain size did not grow significantly. It is found that the pressure can accelerate the densification process. A viscous flow model was used to evaluate the densification mechanism of this sintering process, which showed that the application of external load could provide additional driving force for the densification process and reduce the viscous flow activation energy. The densification mechanism involved is mainly the displacement of powder particles, particle sliding at the particle contact interface, and surface diffusion at the sintering neck. In addition, the Cr-rich phase was precipitated during the densification. Although the final sample obtained from this experiment is not dense, it gives a good perspective on the preparation of nanoscale-grain samples. In the next study, the pressure effect on the grain growth process will be discussed.

Author Contributions: H.Z. performed writing-original draft and investigation. X.T. performed conceptualization, investigation, writing-review and editing, supervision. Q.T. and Z.S. performed investigation. L.L. performed resources. Y.M., J.C., A.L., J.W.C. and C.L. performed review and editing. Y.W. performed conceptualization, supervision and project administration. All authors have read and agreed to the published version of the manuscript.

Funding: This work is supported by the National Natural Science Foundation of China (Grant No. 52020105014, 52001104), the Fundamental Research Funds for the Central Universities (Grant No. PA2021GDSK0090), the Natural Science Foundation of Anhui Province (Grant 1908085ME115), the Natural Science Foundation of Hefei City (Grant No. 2021006) the High Education Discipline Innovation Project (B18018), the International Postdoctoral Exchange Fellowship Program of Helmholtz-OCPC (No. ZD20191015).

Data Availability Statement: Data are contained within the article.

Conflicts of Interest: The authors declare no conflict of interest. The authors declare that they have no known competing financial interests or personal relationships that could have appeared to influence the work reported in this paper.

References

1. Calvo, A.; García-Rosales, C.; Koch, F.; Ordás, N.; Iturriza, I.; Greuner, H.; Pintsuk, G.; Sarbu, C. Manufacturing and testing of self-passivating tungsten alloys of different composition. *Nucl. Mater. Energy* **2016**, *9*, 422–429. [CrossRef]
2. López-Ruiz, P.; Ordás, N.; Iturriza, I.; Walter, M.; Gaganidze, E.; Lindig, S.; Koch, F.; García-Rosales, C. Powder metallurgical processing of self-passivating tungsten alloys for fusion first wall application. *J. Nucl. Mater.* **2013**, *442*, S219–S224. [CrossRef]
3. Calvo, A.; García-Rosales, C.; Ordás, N.; Iturriza, I.; Schlueter, K.; Koch, F.; Pintsuk, G.; Tejado, E.; Pastor, J.Y. Self-passivating W-Cr-Y alloys: Characterization and testing. *Fusion Eng. Des.* **2017**, *124*, 1118–1121. [CrossRef]
4. Fu, T.; Cui, K.; Zhang, Y.; Wang, J.; Shen, F.; Yu, L.; Qie, J.; Zhang, X. Oxidation protection of tungsten alloys for nuclear fusion applications: A comprehensive review. *J. Alloys Compd.* **2021**, *884*, 161057. [CrossRef]
5. Calvo, A.; Schlueter, K.; Tejado, E.; Pintsuk, G.; Ordás, N.; Iturriza, I.; Neu, R.; Pastor, J.Y.; García-Rosales, C. Self-passivating tungsten alloys of the system W-Cr-Y for high temperature applications. *Int. J. Refract. Met. Hard Mater.* **2018**, *73*, 29–37. [CrossRef]

6. Tan, X.Y.; Klein, F.; Litnovsky, A.; Wegener, T.; Schmitz, J.; Linsmeier, C.; Coenen, J.W.; Breuer, U.; Rasinski, M.; Li, P.; et al. Evaluation of the high temperature oxidation of W-Cr-Zr self-passivating alloys. *Corros. Sci.* **2019**, *147*, 201–211. [CrossRef]
7. Litnovsky, A.; Wegener, T.; Klein, F.; Linsmeier, C.; Rasinski, M.; Kreter, A.; Unterberg, B.; Vogel, M.; Kraus, S.; Breuer, U.; et al. Smart alloys for a future fusion power plant: First studies under stationary plasma load and in accidental conditions. *Nucl. Mater. Energy* **2017**, *12*, 1363–1367. [CrossRef]
8. Vilémová, M.; Illková, K.; Lukáč, F.; Matějíček, J.; Klečka, J.; Leitner, J. Microstructure and phase stability of W-Cr alloy prepared by spark plasma sintering. *Fusion Eng. Des.* **2018**, *127*, 173–178. [CrossRef]
9. Sal, E.; García-Rosales, C.; Iturriza, I.; Andueza, I.; Burgos, N. High temperature microstructural stability of self-passivating W-Cr-Y alloys for blanket first wall application. *Fusion Eng. Des.* **2019**, *146*, 1596–1599. [CrossRef]
10. Wang, W.J.; Tan, X.Y.; Yang, S.P.; Mao, Y.R.; Luo, L.M.; Zhu, X.Y.; Litnovsky, A.; Coenen, J.W.; Linsmeier, C.; Wu, Y.C. The influence of powder characteristics on densification behavior and microstructure evolution of W-Cr-Zr alloy consolidated by field-assisted sintering technology. *Int. J. Refract. Met. Hard Mater.* **2022**, *108*, 105939. [CrossRef]
11. Ratzker, B.; Wagner, A.; Sokol, M.; Kalabukhov, S.; Frage, N. Stress-enhanced dynamic grain growth during high-pressure spark plasma sintering of alumina. *Acta Mater.* **2019**, *164*, 390–399. [CrossRef]
12. Omori, M. Sintering, consolidation, reaction and crystal growth by the spark plasma system (SPS). *Mater. Sci. Eng. A* **2000**, *287*, 183–188. [CrossRef]
13. Tokita, M. Progress of Spark Plasma Sintering (SPS) Method, Systems, Ceramics Applications and Industrialization. *Ceramics* **2021**, *4*, 160–198. [CrossRef]
14. Liu, D.G.; Zheng, L.; Luo, L.M.; Zan, X.; Song, J.-P.; Xu, Q.; Zhu, X.Y.; Wu, Y.C. An overview of oxidation-resistant tungsten alloys for nuclear fusion. *J. Alloys Compd.* **2018**, *765*, 299–312. [CrossRef]
15. Madeira, S.; Buciumeanu, M.; Carvalho, O.; Silva, F.S. Influence of sintering pressure on the microstructure and tribological properties of low temperature fast sintered hot-pressed Y-TZP. *Ceram. Int.* **2019**, *45*, 5883–5893. [CrossRef]
16. Antou, G.; Guyot, P.; Pradeilles, N.; Vandenhende, M.; Maître, A. Identification of densification mechanisms of pressure-assisted sintering: Application to hot pressing and spark plasma sintering of alumina. *J. Mater. Sci.* **2014**, *50*, 2327–2336. [CrossRef]
17. Borkar, T.; Banerjee, R. Influence of spark plasma sintering (SPS) processing parameters on microstructure and mechanical properties of nickel. *Mater. Sci. Eng. A* **2014**, *618*, 176–181. [CrossRef]
18. Wang, D.; Yuan, H.; Qiang, J. The Microstructure Evolution, Mechanical Properties and Densification Mechanism of TiAl-Based Alloys Prepared by Spark Plasma Sintering. *Metals* **2017**, *7*, 201. [CrossRef]
19. Li, W.; Zeng, F.; Li, L.; Wang, Z.; Liu, H.; Peng, Y.; Gu, Y. Spark plasma sintering of Ti–1Al–8V–5Fe alloy: Densification mechanism and grain growth. *Appl. Phys. A* **2020**, *126*, 709. [CrossRef]
20. Yang, S.P.; Wang, W.J.; Tan, X.Y.; Zhu, H.J.; Litnovsky, A.; Klein, F.; Mao, Y.R.; Coenen, J.W.; Linsmeier, C.; Luo, L.M.; et al. Influence of the applied pressure on the microstructure evolution of W-Cr-Y-Zr alloys during the FAST process. *Fusion Eng. Des.* **2021**, *169*, 112474. [CrossRef]
21. Wang, W.J.; Tan, X.Y.; Yang, S.P.; Luo, L.M.; Zhu, X.Y.; Mao, Y.R.; Litnovsky, A.; Coenen, J.W.; Linsmeier, C.; Wu, Y.C. On grain growth and phase precipitation behaviors during W-Cr-Zr alloy densification using field-assisted sintering technology. *Int. J. Refract. Met. Hard Mater.* **2021**, *98*, 105552. [CrossRef]
22. Vilémová, M.; Lukáč, F.; Veverka, J.; Illková, K.; Matějíček, J. Controlling the carbide formation and chromium depletion in W-Cr alloy during field assisted sintering. *Int. J. Refract. Met. Hard Mater.* **2019**, *79*, 217–223. [CrossRef]
23. Wang, W.J.; Tan, X.Y.; Liu, J.Q.; Chen, X.; Wu, M.; Luo, L.M.; Zhu, X.Y.; Chen, H.Y.; Mao, Y.R.; Litnovsky, A.; et al. The influence of heating rate on W-Cr-Zr alloy densification process and microstructure evolution during spark plasma sintering. *Powder Technol.* **2020**, *370*, 9–18. [CrossRef]
24. Davidson, S.; Perkin, M. An investigation of density determination methods for porous materials, small samples and particulates. *Measurement* **2013**, *46*, 1766–1770. [CrossRef]
25. Ghafuri, F.; Ahmadian, M.; Emadi, R.; Zakeri, M. Effects of SPS parameters on the densification and mechanical properties of TiB_2-SiC composite. *Ceram. Int.* **2019**, *45*, 10550–10557. [CrossRef]
26. Diouf, S.; Molinari, A. Densification mechanisms in spark plasma sintering: Effect of particle size and pressure. *Powder Technol.* **2012**, *221*, 220–227. [CrossRef]
27. Wei, X.; Giuntini, D.; Maximenko, A.L.; Haines, C.D.; Olevsky, E.A.; Kang, S.J. Experimental Investigation of Electric Contact Resistance in Spark Plasma Sintering Tooling Setup. *J. Am. Ceram. Soc.* **2015**, *98*, 3553–3560. [CrossRef]
28. Grasso, S.; Sakka, Y.; Maizza, G. Pressure Effects on Temperature Distribution during Spark Plasma Sintering with Graphite Sample. *Mater. Trans.* **2009**, *50*, 2111–2114. [CrossRef]
29. Kim, H.-T.; Kawahara, M.; Tokita, M.; Metallurgy, P. Specimen temperature and sinterability of Ni powder by spark plasma sintering. *J. Jpn. Soc. Powder Powder Metall.* **2000**, *47*, 887–891. [CrossRef]
30. Klueh, R.L.; Maziasz, P.J. The microstructure of chromium-tungsten steels. *Metall. Trans. A* **1989**, *20*, 373–382. [CrossRef]
31. Huang, L.; Pan, Y.; Zhang, J.; Du, Y.; Zhang, Y.; Zhang, S. Densification, grain growth mechanism and mechanical properties of Mo 10Nb refractory targets fabricated by SPS. *Int. J. Refract. Met. Hard Mater.* **2021**, *99*, 105575. [CrossRef]
32. Du, Z.-Y.; Lv, Y.-Q.; Han, Y.; Fan, J.-L.; Ye, L. Sintering densification behavior and kinetic mechanism of nano-tungsten powder prepared by sol-spray drying. *Tungsten* **2021**, *2*, 371–380. [CrossRef]

33. Zhang, Z.H.; Wang, F.C.; Lee, S.K.; Liu, Y.; Cheng, J.W.; Liang, Y. Microstructure characteristic, mechanical properties and sintering mechanism of nanocrystalline copper obtained by SPS process. *Mater. Sci. Eng. A* **2009**, *523*, 134–138. [CrossRef]
34. Li, X.X.; Yang, C.; Lu, H.Z.; Luo, X.; Li, Y.Y. Correlation between atomic diffusivity and densification mechanism during spark plasma sintering of titanium alloy powders. *J. Alloys Compd.* **2019**, *787*, 112–122. [CrossRef]
35. Li, X.X.; Yang, C.; Chen, T.; Zhang, L.C.; Hayat, M.D.; Cao, P. Influence of powder shape on atomic diffusivity and resultant densification mechanisms during spark plasma sintering. *J. Alloys Compd.* **2019**, *802*, 600–608. [CrossRef]
36. Ristic, M.; Milosevic, S. Frenkel's theory of sintering. *Sci. Sinter.* **2006**, *38*, 7–11. [CrossRef]
37. Barick, P.; Chakravarty, D.; Saha, B.P.; Mitra, R.; Joshi, S.V. Effect of pressure and temperature on densification, microstructure and mechanical properties of spark plasma sintered silicon carbide processed with β-silicon carbide nano-powder and sintering additives. *Ceram. Int.* **2016**, *42*, 3836–3848. [CrossRef]
38. Yang, C.; Zhu, M.D.; Luo, X.; Liu, L.H.; Zhang, W.W.; Long, Y.; Xiao, Z.Y.; Fu, Z.Q.; Zhang, L.C.; Lavernia, E.J. Influence of powder properties on densification mechanism during spark plasma sintering. *Scr. Mater.* **2017**, *139*, 96–99. [CrossRef]
39. Song, X.; Liu, X.; Zhang, J. Neck Formation and Self-Adjusting Mechanism of Neck Growth of Conducting Powders in Spark Plasma Sintering. *J. Am. Ceram. Soc.* **2006**, *89*, 494–500. [CrossRef]
40. Helle, A.S.; Easterling, K.E.; Ashby, M.F. Hot-isostatic pressing diagrams: New developments. *Acta Metall.* **1985**, *33*, 2163–2174. [CrossRef]
41. Chaim, R.; Levin, M.; Shlayer, A.; Chaim, R.; Levin, M.; Shlayer, A.; Estournes, C. Sintering and densification of nanocrystalline ceramic oxide powders: A review. *Adv. Appl. Ceram.* **2013**, *107*, 159–169. [CrossRef]
42. Chaim, R.; Marder, R.; Estournés, C.; Shen, Z. Densification and preservation of ceramic nanocrystalline character by spark plasma sintering. *Adv. Appl. Ceram.* **2013**, *111*, 280–285. [CrossRef]